Environ Fluid Mech
DOI 10.1007/s10652-011-9220-5

ORIGINAL ARTICLE

A coupled numerical model to investigate the air–sea interaction at the coastal upwelling area of Cabo Frio, Brazil

Flávia Noronha Dutra Ribeiro · Jacyra Soares · Amauri Pereira de Oliveira

Received: 8 March 2010 / Accepted: 8 August 2011

Abstract This work investigates the capability of an oceanic numerical model dynamic and thermodynamically coupled to a three-dimensional mesoscale atmospheric numerical model to simulate the basic features of the air–sea interaction in the coastal upwelling area of Cabo Frio (RJ, Brazil). The upwelling/downwelling regime is an important feature in the oceanic circulation of Cabo Frio and determines the sustainability of local ecosystems. This regime is predominantly driven by the atmospheric circulation and is well documented, being suitable to be used as test reference for atmospheric and oceanic coupled and uncoupled models. The oceanic boundary conditions, coastline shape and coupling effect have been tested. The uncoupled oceanic model forced by a NE (SW) wind field generates a realistic upwelling (downwelling) phenomenon regardless of the proximity of the lateral boundary and how realistic is the shape of the coastline. The atmospheric-oceanic coupled model generates an upwelling location and intensity similar to the uncoupled simulation, but the upwelling is gradually enhanced by the sea-breeze circulation. It also generates vertical profiles of mixing ratio that compare better to the observations than the uncoupled simulation and air potential temperature and wind vertical profiles that represent particular features of the atmospheric circulation at Cabo Frio.

Keywords Coupled numerical model · Coastal upwelling · Air–sea interaction · Open boundary conditions

1 Introduction

The southeast coast of Brazil (21°–27°S, 40°–47°W) very often presents the phenomenon of coastal upwelling due mainly to the atmospheric circulation associated to the South Atlantic Subtropical High (SASH). This high pressure system generates northeasterly surface winds, which are favorable to the development of the coastal upwelling, over the Brazilian

F. N. D. Ribeiro · J. Soares (✉) · A. P. de Oliveira
Department of Atmospheric Sciences, University of São Paulo, São Paulo, Brazil
e-mail: jacyra@usp.br

Published online: 06 September 2011

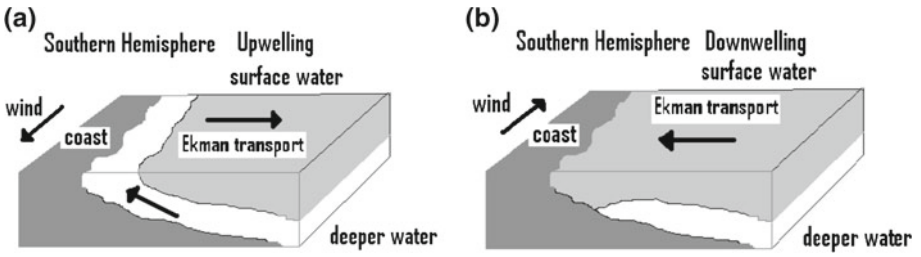

Fig. 1 Scheme of the Ekman transport during **a** coastal upwelling favorable wind and **b** coastal downwelling favorable wind

Southeast coast. This phenomenon occurs when the wind has an intense component parallel to the coast with the coast at its right (left) side at the Southern (Northern) Hemisphere. With time, due to the Coriolis Effect, surface water is transported away from the coast (Ekman transport), allowing deeper and colder water to surface (Fig. 1a). Therefore, the upwelling is characterized by cold anomalies of sea surface temperature (SST). When the wind blows in the opposite direction, the Ekman transport is from the ocean to the coast, causing the SST to increase (Fig. 1b). At Cabo Frio, located at the southeast coast of Brazil (22.87°S, 42.02°W), it happens mainly during the passage of cold fronts, when the wind direction at the surface changes counterclockwise and blows from southwest for approximately 1 day after the passage of the front [1]. Therefore, southwesterly winds disrupt the coastal upwelling at Cabo Frio, which is progressively substituted by a downwelling regime (Fig. 1b). Factors like coastline geometry and bottom topography cause the region of Cabo Frio to have the strongest coastal upwelling event of the Brazilian Southeast coast [2].

Coastal upwelling is a very important phenomenon because it brings nutrient-rich water to the coast [3,4] improving fishery activities [5]. Alkenone-based temperature analysis indicated that upwelling cooling patterns in the Cabo Frio area have intensified over the last 700 years [6]. The colder SST may also have an impact on local atmospheric processes such as sea-breeze, influencing weather conditions and also pollutant transport and deposition [7–11]. However, only few works have investigated the air–sea interaction at Cabo Frio area and its impact on the local patterns of weather and climate.

The coastal upwelling phenomenon at Cabo Frio was previously simulated by some researchers, but none of them used coupled atmospheric and oceanic models. Rodrigues and Lorenzzetti [2] used a 2-layer finite-element oceanic model to investigate the effects of bottom topography and coastline geometry on the coastal upwelling of the continental shelf at the southeast of Brazil. By integrating the model for 5 days with a constant NE wind field in three different experiments (the first one with real topography and real coastline, the second one with flat bottom and real coastline and the third one with real topography and smoothed coastline), they observed that the first experiment reproduced the upwelling reasonably well with respect to location and magnitude. They also noticed that coastline irregularities are important in the location of the upwelling cores at the southern portion of the continental shelf and that the bottom topography was responsible for the location of the upwelling cell at the northern portion. It was concluded that the coastline irregularities dominate over topographic variations in defining the location of the coastal upwelling at Cabo Frio.

Carbonel [12] developed a 1½ layer finite difference oceanic model to investigate the upwelling and downwelling events caused by successive changes in the wind field, using Cabo Frio as a case study. The change of SST was reproduced with a good degree of approximation and the model was able to reproduce the evolution time of SST during upwelling–

downwelling cycles. This model was coupled to a biological numerical model by Carbonel and Valentin [4] to investigate the bloom of phytoplankton in the upwelling ecosystem of Cabo Frio.

To study the effect of coastal upwelling on the sea-breeze circulation at Cabo Frio, Franchito et al. [13] used a three-dimensional non-linear primitive equation atmospheric model with the SST held constant and homogeneous. Four experiments were performed simulating summer, fall, winter and spring periods, and the generated wind fields were then used to force a 2 layer finite-element oceanic model. The atmospheric model results showed that when the upwelling phenomenon is stronger and produces a higher gradient of temperature between the ocean and the continent, the sea-breeze is also stronger. The oceanic model results showed that when the wind field generated by the atmospheric model is combined to a constant NE wind of $6\,\mathrm{ms}^{-1}$, the upwelling is enhanced. Therefore, the results suggest that there is a positive feedback between the upwelling and the sea-breeze at Cabo Frio.

The objective of this work is investigating the capability of an oceanic numerical model dynamically and thermodynamically coupled to a three-dimensional mesoscale atmospheric numerical model (Topographic Vorticity mode Mesoscale-Non Hydrostatic, TVM-NH) to simulate the basic features of air–sea interaction in the coastal upwelling area of Cabo Frio (RJ, Brazil). It should be emphasized that, to the authors' knowledge, this is the first attempt to dynamic and thermodynamically couple oceanic and atmospheric models to investigate the upwelling phenomenon at Cabo Frio.

2 Investigated region

The coastline of the investigated area is shown on Fig. 2. It is located in Rio de Janeiro (RJ, Brazil), where there are two capes: Cabo Frio and Cabo de São Tomé. Westward of both capes there are frequently areas of cold water, but the lowest SST area is usually found near the coast just west of Cabo Frio [2,14].

The coastline from Cabo de São Tomé to Cabo Frio is oriented NE–SW. The continental shelf has the same orientation and it is about 100 km long, 70–100 km wide and 80–100 m deep at the shelf break. Southward of Cabo Frio, the coastline and the isobath orientation changes to E–W. The shelf is about 400 km long, 70–150 km wide and 140–180 m deep [1].

In the investigated region there are three different water masses: the coastal water, located at the continental shelf and characterized by high temperatures and low salinity; the tropical

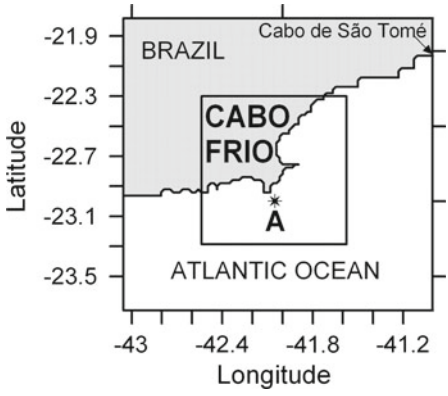

Fig. 2 Domain and coastline considered by the numerical models. The central *square* illustrates the region discussed at the "Results". The *star* symbol indicates the point "A", where were performed atmospheric vertical profiles considered at the results

water, located at the upper part of the water column and characterized by temperatures above 20°C; and the South Atlantic Central Water (SACW), located at the lower part of the water column and identified by temperatures below 20°C. When the coastal upwelling occurs the SACW may surface, causing the SST to drop as low as 10°C [1].

According to Castro [15], the circulation at the portion of the continental shelf located in this area is mainly forced by the wind. In this region, the prevailing wind blows from NE during the whole year because of the presence of the SASH. This pattern is changed by the passage of cold fronts, which usually occurs every 5–10 days. The frequency of these passages is higher during the winter than the summer [15].

Amor [1], performing climatology studies and numeric experiments, concluded that the intrusion of the SACW into the continental platform is strongly modulated on seasonal scale by the wind associated to the seasonal oscillations of SASH center over the South Atlantic Ocean. The northeasterly wind favors the permanent intrusion of SACW at the continental shelf on a sub-inertial scale; the cold front passages promote the diminishing of the SACW intrusion for 1–2 days and the very intense southwesterly wind may partially remove the SACW intrusion from the continental shelf for 1 day.

Leite [16] compared currents measured by an Acoustic Doppler Current Profiler (ADCP) with the wind field obtained by a meteorological buoy and by QuickSCAT scatterometer and observed that the currents are directly influenced by the wind field, proving that the wind is the main force on the currents at Cabo Frio.

Oda [17] performed radiosonde soundings to evaluate the atmospheric boundary layer depth in the Cabo Frio region. The results showed that the atmospheric boundary layer is more stable during the occurrence of upwelling and suggested a positive feedback between the coastal upwelling and the sea-breeze circulation, as suggested by Franchito et al. [13].

Dourado and Oliveira [18] investigated through observational data the evolution of the vertical extent of the atmospheric and the oceanic boundary layers at Cabo Frio during the passage of a cold front in 1992. A deepening of both boundary layers was observed, as the upwelling was disrupted by the cold front passage. Later on, a one-dimension atmospheric second-order closure model thermodynamically coupled to an oceanic mixed layer model was used to investigate the short term variation of the atmospheric and oceanic boundary layers at Cabo Frio, taking as reference the observations performed before [19]. When compared to the observations, the model results indicated that the thermal contrast (ocean surface warmer than lower atmosphere) is not strong enough to generate oceanic and atmospheric boundary layers as deep as observed during the passage of the cold front. Other mechanisms like convective turbulent mixing in the ocean, associated with the cooling of the surface and the warming of the oceanic bottom boundary layer and the effect of surface waves may have important roles in the deepening of both oceanic and atmospheric boundary layers.

As indicated by the review above, all numerical investigations carried out to simulate the interaction between air and ocean at the Cabo Frio upwelling region did not dynamically couple the ocean to the atmosphere. The only study that couples the atmosphere to the ocean did it thermodynamically [18], and it was carried using a one-dimensional model. Thus, it did not have horizontal structure and could not relate mass to wind in the atmosphere or current in the ocean as expected in the dynamical coupling. Therefore, the present work, that couples a three-dimensional mesoscale atmospheric model to a two-dimensional ocean model, is the first attempt to address the air–sea interaction by coupling atmosphere and ocean thermodynamically and dynamically.

3 Numerical models

The oceanic and atmospheric models used in this work are described below.

3.1 Oceanic numerical model

The oceanic model developed here is a 1½ layer model and followed the description of the one developed by Carbonel [12]. The concept of a 1½ layer ocean model is well known and documented in literature since the early 1970s [20–25]. It has a lower inert layer with constant temperature $\left(T^l\right)$ and no pressure gradients, and an upper layer where the governing equations are the vertically-integrated non-linear equations of momentum, continuity and transport of SST.

The equations are similar to the ones used by Carbonel [12], as follows:

$$\frac{\partial \mathrm{U}}{\partial t}+\frac{\partial \mathrm{uU}}{\partial x}+\frac{\partial \mathrm{vU}}{\partial y}-f\mathrm{V}+gh\left\{\sigma\frac{\partial h}{\partial x}+\frac{h\theta}{2\overline{\mu}}\frac{\partial SST}{\partial x}\right\}+r\mathrm{U}-\frac{\tau_x}{\rho^{\mathrm{u}}}=0 \tag{1}$$

$$\frac{\partial \mathrm{V}}{\partial t}+\frac{\partial \mathrm{uV}}{\partial x}+\frac{\partial \mathrm{vV}}{\partial y}+f\mathrm{U}+gh\left\{\sigma\frac{\partial h}{\partial y}+\frac{h\theta}{2\overline{\mu}}\frac{\partial SST}{\partial y}\right\}+r\mathrm{V}-\frac{\tau_y}{\rho^{\mathrm{u}}}=0 \tag{2}$$

$$\frac{\partial h}{\partial t}+\frac{\partial \mathrm{U}}{\partial x}+\frac{\partial \mathrm{V}}{\partial y}-w_e=0 \tag{3}$$

$$\frac{\partial SST}{\partial t}+\mathrm{u}\frac{\partial SST}{\partial x}+\mathrm{v}\frac{\partial SST}{\partial y}+\frac{1}{h}(s+Q)=0 \tag{4}$$

where h is the upper layer thickness, u and v are the velocity components in the x and y directions respectively, U and V are the transport components (U = hu; V = hv) , f is the Coriolis parameter; g is the gravity acceleration, SST is the sea surface temperature, r is the Rayleigh friction coefficient, θ is the thermal expansion coefficient and the density coefficients are defined as, $\sigma = 1-\mu, \overline{\mu} = \frac{\mu}{(\mu-\sigma)}$ and $\mu = \frac{\rho^u}{\rho^l}$, where ρ^u is the upper layer density and ρ^l is the lower layer density.

The entrainment velocity (w_e) is defined as: $w_e = \frac{(H_i-h)^2}{t_e H_e}$ when $h \leq H_e$ and $w_e = 0$ otherwise. H_e is the entrainment layer thickness, t_e is the entrainment time scale, H_i is the initial upper layer thickness.

The source or sink of heat across the interface (s) is defined as $s = H_i\frac{\partial \mathrm{U}}{\partial x}\left(\frac{SST-T^l}{h}\right)+H_i\frac{\partial \mathrm{V}}{\partial y}\left(\frac{SST-T^l}{h}\right)$, where T^l is the constant temperature of the lower layer.

The surface heat flux, Q, is defined as:

$$Q=-\frac{H_i^2}{t_s}\left(\frac{T^u-SST}{h}\right) \tag{5}$$

where T^u is the initial temperature of the upper layer and t_s is the time for the upper layer to relax back to the initial temperature T^u.

When the oceanic model is not coupled to the atmospheric model, the component of the wind stress is defined as:

$$\tau_i=\rho^{air}C_D w_i\,|W|_{i=x,y} \tag{6}$$

where ρ^{air} is the air density, W is the wind velocity intensity at a reference height, w_i is the wind component in the direction i and C_D is the drag coefficient.

When the models are coupled, the surface heat flux Q and the wind stress τ_i are provided by the atmospheric model.

3.1.1 Boundary conditions

At the coastline, the velocity and transport components normal to the boundary are set to zero and the zero gradient condition is applied to the upper layer thickness and to the SST values.

At open boundaries is used the weakly-reflective boundary condition described by Verboom and Slob [26] and also discussed by Van Dongeren and Svendsen [27]. This condition is based on the characteristic method; the characteristics are curves at the x–y plane through which the information at the boundaries is propagated. The system formed by Eqs. 1–3 is a non-linear hyperbolic system; therefore it has two characteristic equations. The general solution of the system contains progressive waves which cannot be completely uncoupled, so it is not possible to derivate a truly non-reflective boundary condition. Verboom and Slob [26] developed a weakly-reflective boundary condition by applying transformations that decouple the ingoing waves from the outgoing waves up to the desired order of approximation.

This boundary condition is applied on the axis normal to the boundary (n), as follows:

$$\frac{\partial\left(\mathrm{U}_n \pm ch\right)}{\partial t} + c\frac{\partial\left(\mathrm{U}_n \pm ch\right)}{\partial x_n} \pm c\left(w_e\right) + \frac{\partial\left(\mathrm{u}_n\mathrm{U}_n\right)}{\partial x_n} + \varepsilon_n + \frac{gh^2\theta}{2\overline{\mu}}\frac{\partial SST}{\partial x_n} - \frac{\tau_n}{\rho^u} + r\mathrm{U}_n = 0 \tag{7}$$

where $c = \sqrt{\sigma g h}$ is the characteristic velocity. The sign of c is chosen at each boundary to define the ingoing characteristic equation for each case.

The numeric approximation used in this model is finite difference, forward in time (k) with a dissipative interface and centered in space, as follows:

$$\phi^k\left(f_{i,j}^k\right) = \frac{\left(f_{i,j}^{k+1} - f_{i,j}^*\right)}{\Delta t} \tag{8}$$

$$\alpha_i\left(f_{i,j}^k\right) = \frac{\left(f_{i+1,j}^k - f_{i-1,j}^k\right)}{2\Delta x} \tag{9}$$

where ϕ^k is the forward in time finite-difference operator, α_i is the centered in space finite-difference operator and f^* is the dissipative interface defined as:

$$f_{i,j}^* = \frac{1}{8}f_{i+1,j}^l + \frac{1}{8}f_{i-1,j}^l + \frac{1}{2}f_{i,j}^l + \frac{1}{8}f_{i,j+1}^l + \frac{1}{8}f_{i,j-1}^l \tag{10}$$

The velocity (u) and transport (U) values are placed at the grid cell between the grid points (i, j) and $(i, j + 1)$; v and V are placed between (i, j) and $(i + 1, j)$; SST and the thickness (h) are placed at the center of the grid cell, as shown in Fig. 3.

The numerical approximations of Eqs. 1–4 used here are:

$$\phi^k\left(\mathrm{U}_{i,j}^k\right) + \alpha_i\left((\mathrm{uU})_{i,j}^k\right) + \alpha_j\left((\overline{\mathrm{v}}\mathrm{U})_{i,j}^k\right) + g\overline{h}_{i,j}^k\overline{p_x}_{i,j}^k - f\overline{\mathrm{V}}_{i,j}^k + r\mathrm{U}_{i,j}^k - \frac{\tau_{xi,j}^k}{\rho^u} = 0 \tag{11}$$

$$\phi^k\left(\mathrm{V}_{i,j}^k\right) + \alpha_i\left((\overline{\mathrm{u}}\mathrm{V})_{i,j}^k\right) + \alpha_j\left((\mathrm{vV})_{i,j}^k\right) + g\overline{h}_{i,j}^k\overline{p_y}_{i,j}^k + f\overline{\mathrm{U}}_{i,j}^k + r\mathrm{V}_{i,j}^k - \frac{\tau_{yi,j}^k}{\rho^u} = 0 \tag{12}$$

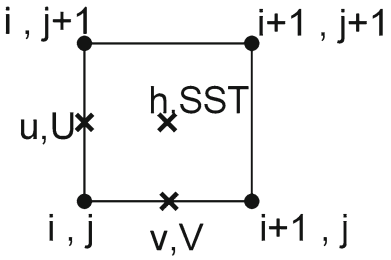

Fig. 3 Scheme of variable positions on the grid cell

$$\phi^k\left(h_{i,j}^k\right)+\alpha_i\left(\overline{\mathrm{U}}_{i,j}^k\right)+\alpha_j\left(\overline{\mathrm{V}}_{i,j}^k\right)-w_{ei,j}^k=0 \tag{13}$$

$$\phi^k\left(SST_{i,j}^k\right)+\overline{\mathrm{u}}\alpha_i\left(SST_{i,j}^k\right)+\overline{\mathrm{v}}\alpha_j\left(SST_{i,j}^k\right)+\frac{\left(s_{i,j}^k+Q_{i,j}^k\right)}{h_{i,j}^k}=0 \tag{14}$$

where $\overline{p_x}=\sigma\alpha_i\left(\overline{h}_{i,j}^k\right)+\frac{\overline{h}_{i,j}^k\theta\alpha_i\left(\overline{SST}_{i,j}^k\right)}{2\overline{\mu}}$ and $\overline{p_y}=\sigma\alpha_j\left(\overline{h}_{i,j}^k\right)+\frac{\overline{h}_{i,j}^k\theta\alpha_j\left(\overline{SST}_{i,j}^k\right)}{2\overline{\mu}}$ are the pressure components in function of h and SST.

The variables with bars are spatial averages. They are a better approximation of the value of each variable at the point of calculation, when its value is positioned elsewhere (Fig. 3). Therefore, one additional grid point at each boundary is necessary to allow the evaluation of the variables mean value at the boundaries. The lateral space finite-difference operator (λ_b) used at the open boundaries is defined as:

$$\lambda_b\left(f_b^k\right)=\frac{\left(3f_b^k-4f_{b-1}^k+f_{b-2}^k\right)}{2\Delta x} \tag{15}$$

where b is the boundary point and b − 1 and b − 2 are the interior points in an axis normal to the boundary.

Then the boundary condition in Eq. 5 becomes:

$$\begin{aligned}&\phi^k\left(\mathrm{U}_{nb}^k\pm\overline{ch}_b^k\right)+\overline{c}_b^k\lambda_b\left(\mathrm{U}_{nb}^k\pm\overline{ch}_b^k\right)\pm\overline{c}_b^k\left(-\overline{w_e}_b^k\right)+\lambda_b\left(u_b^k\mathrm{U}_b^k\right)\\&+\varepsilon_b+\frac{g\overline{h}_b^{k2}\theta}{2\overline{\mu}}\lambda_b\left(\overline{SST}_b^k\right)-\frac{\tau_{nb}^k}{\rho^u}+r\mathrm{U}_b^k=0\end{aligned} \tag{16}$$

The constant parameter values in (1)–(16) are similar to those used by Carbonel [12] and are listed in Table 1.

Finally, the numerical solution of the equations described above is carried out through the following steps: first, the heat exchanges (s and Q) are calculated; next the SST; then the pressure (p); after that, the transport components (U and V); and at the end, the thickness of the active layer (h). The current components are then obtained by the division of the transport components by the thickness h.

3.1.2 Initial conditions

The initial SST was 26°C and the initial surface layer thickness was 30 m. The initial transport and velocity components were zero and the initial wind stress was calculated by Eq. 6 with a NE wind of 6 ms^{-1}.

Table 1 Constant parameters of the oceanic model

Parameter	Notation	Value
Initial upper layer thickness	H_i	30 m
Entrainment layer thickness	H_e	20 m
Upper layer density	ρ^u	1023 kg m^{-3}
Lower layer density	ρ^l	1026.7 kg m^{-3}
Coriolis parameter	f	-5.68×10^{-5} s^{-1}
Wind drag coefficient	C_D	2.0×10^{-3}
Air density	ρ^{air}	1.2 kg m^{-3}
Rayleigh friction coefficient	R	1.8×10^{-6} s^{-1}
Initial upper layer temperature	T^u	26°C
Lower layer temperature	T^l	14°C
Thermal expansion coefficient	θ	3.0×10^{-4}°C^{-1}
Entrainment time scale	t_e	1/2 days
Surface heat flux time scale	t_s	12 days
Grid step	Δx	1800 m
Time step	Δt	600 s

3.2 Atmospheric numerical model

The series of models called Topographic Vorticity Model (TVM) began with the two dimensional model 'URBMET' developed by Bornstein [28]. Subsequently, URBMET was expanded to three dimensions and the topographic effects were incorporated using the vorticity equations in sigma-Z coordinate system. This version was called TVM [29,30] and classified as mesoscale-β model [31,32]. Thunis and Clappier [33] developed the non-hydrostatic version of TVM (TVM-NH). The TVM-NH was successfully used to simulate the local circulation in the Iberian Peninsula [34,35]. In Brazil, the TVM has successfully been applied to simulate atmospheric boundary layer circulation [36–40].

The TVM-NH model is three-dimensional, follows the Boussinesq approximations of the vorticity equations obtained from the basic Reynolds-averaged equations of motion and uses sigma coordinates to accommodate topography over land. The vorticity approach cut the pressure and density variables out of the equations.

The vertical grid is structured as follows: surface parameters at the bottom boundary; the first layer is the surface boundary layer (SBL), where the meteorological parameters are obtained by similarity theory equations and the other layers are governed by finite difference approximations of the vorticity, thermodynamic and mass conservation of moisture equations.

The surface parameters are determined in the following order: first, the model evaluates solar and infrared radiative fluxes and calculates the net radiation R_N; then it obtains the residual heat flux R as:

$$R = R_N - SH - LH \tag{17}$$

where SH is the sensible heat flux and LH is the latent heat flux from the previous step. On the continent, the residual heat flux represents the soil heat flux (G) and on the ocean it represents the ocean heat flux (Q_{ocean}).

Over land the surface temperature is computed by the force-restore method of Deardorff [41,42] and the specific humidity is computed using the Penmann–Monteith method. For water, when the models are coupled, time and spatial evolution of SST is provided by the oceanic model, calculated by Eq. 4. When the atmospheric model is uncoupled, the water temperature is held constant and homogeneous. The specific humidity near the surface above the water (1 mm) is defined as the saturation value for the temperature of the water.

The SBL fluxes are then evaluated as:

$$\begin{aligned} \tau &= -\rho^{air} u_*^2 \\ SH &= -\rho^{air} C_p u_* \theta_* \\ LH &= -\rho^{air} L_v u_* q_* \end{aligned} \tag{18}$$

where τ is the wind stress, ρ^{air} is the air density, C_p is the specific heat at constant pressure, L_v is the latent heat of water vaporization, u_* is the friction velocity, θ_* is the characteristic potential temperature scale and q_* is the characteristic scale of specific humidity.

The SBL flux values are then used to force the dynamic, thermodynamic and moisture conservation equations at the other layers of the domain: the turbulent kinetic energy equation is solved; the diffusion coefficient profiles are obtained; potential temperature, specific humidity and horizontal vorticity equations are solved; the stream functions and velocity components are updated; time is advanced and the cycle is repeated. A detailed model description can be found in [33].

The domain of the atmospheric model used in this work was based in a horizontal area of 99 km × 99 km, delimited by the inner square on Fig. 2, with a grid spacing of 3 km × 3 km (34 × 34 grid points). At each lateral boundary there are eight grid points, with a variable grid spacing from 3.6 to 12.9 km following a geometric progression at 1.2 ratio, totalizing the 205 km × 205 km domain, with 50 × 50 grid points (external square on Fig. 2), in order to minimize the influence of the boundaries on the studied area [11]. This area is large enough to study ABL processes in a region with sea breeze [11,40,43]. In the vertical direction, 25 grid points are used and the grid size varies from 15 m at the first level to 1200 m at the top of the model, allowing a better resolution near the surface. The TVM-NH atmospheric model was successfully used by researchers at coastal areas to investigate mesoscale atmospheric processes such as sea-breeze [11,43] and lake-breeze [40].

3.2.1 Boundary conditions

The boundary conditions at the four lateral boundaries are zero-gradient, the horizontal wind field is considered geostrophic at the top of the domain and the vorticity, turbulent kinetic energy and the vertical variation of the vertical velocity component are zero. At the bottom of the model, the velocity components are zero and the turbulent fluxes are calculated as described above.

The topography used by the model is presented at Fig. 4. The maximum height—1529 m—is located at 22°26′S of latitude and 42°64′W of longitude at the northwestern part of the domain. Near the coast the topography is almost flat.

The land-use type defines the parameters for the calculation of surface temperature, humidity and superficial fluxes. Only one land-use type was defined besides water, because tests performed with more than one land-use type did not present significantly different results (not shown here). The land-use type utilized here is classified as agriculture or cropland/natural vegetation mosaic (IGBP classification) [44], corresponding to the predominant type at the continental region of Cabo Frio.

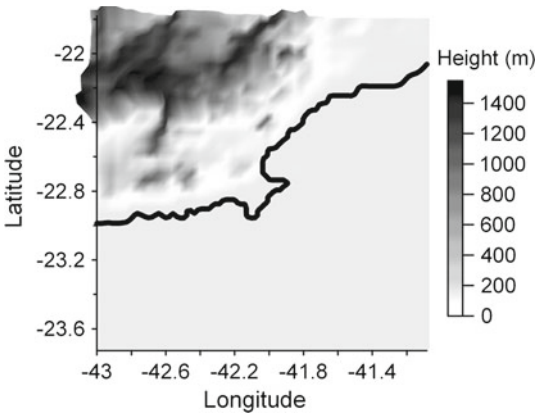

Fig. 4 Topography of the investigated area

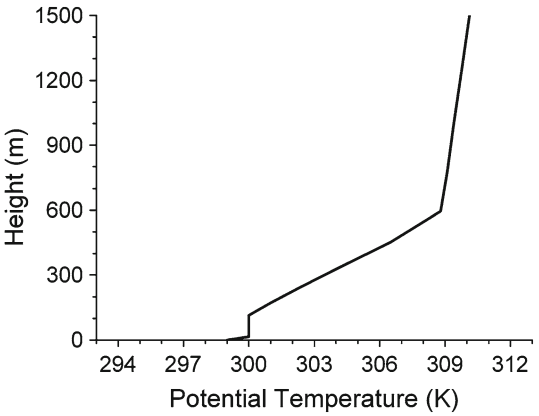

Fig. 5 Initial air potential temperature vertical profile

3.2.2 Initial conditions

The initial air potential temperature (Fig. 5) and the initial specific humidity profiles were based on the sounding taken by Oda [17], at 01/09/1995, in (22.97°S, 42.03°W).

The initial specific humidity value near the surface is 16.8 g kg^{-1} and its vertical profile was assumed to be logarithmic.

The wind value used as initial condition corresponds to a large scale wind, referred here as geostrophic wind. Its vertical profile was defined by a zonal component of -4.24 ms^{-1} and a meridional component of -4.24 ms^{-1}, totalizing a NE wind of 6 ms^{-1} at all heights, except at the surface, where the wind is set to zero. The wind intensity was obtained by the average of hourly measurements taken at the Meteorological Station of Cabo Frio (22.88°S, 42.02°W), at 10 m of altitude, by the Navigation and Hydrography Directorate of the Brazilian Navy, between 1970 and 1980.

The simulations started at 00 LT, but the results were analyzed only after 06 LT so that the initial variables, considered horizontally homogeneous, had time to adjust themselves to the spatial differences.

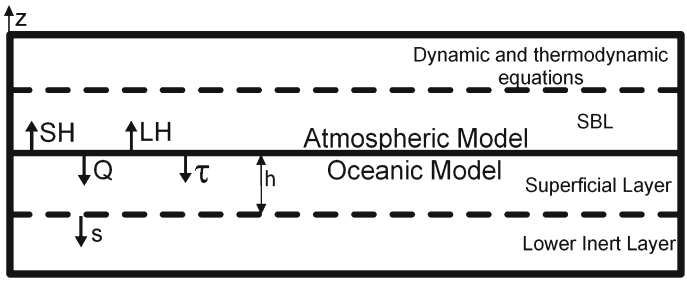

Fig. 6 Scheme of the models coupling. SH and LH are, respectively, the sensible heat and the latent heat fluxes. Q and τ are, respectively, the surface heat flux and the momentum flux from the atmosphere to the ocean, s is source or sink of heat across the interface and h is the thickness of the oceanic superficial layer

3.3 Coupling between the oceanic and atmospheric models

The oceanic model was developed in the form of a subroutine and set to use the same horizontal grid spacing as the TVM-NH model. When the atmospheric model starts, it calls the oceanic model subroutine, which returns a 2-day integration SST field. At this point, the oceanic model is still uncoupled and therefore it is forced by a constant 6 ms^{-1} NE winds through Eq. 6. The surface heat flux is calculated by Eq. 5. The period of 2 days was chosen because it is enough time for the upwelling phenomenon to be well established in the region, since it was shown by Ikeda et al. [14] that the time elapsed between the onset of NE winds of magnitude greater than 5 ms^{-1} and the first appearance of colder upwelling water is about 24 h. Then the SST field is used by the TVM-NH model to determine the surface heat fluxes over the ocean. The time step of the TVM-NH and the oceanic models are, respectively, 30 and 600 s. Therefore, the SST field remains the same for 20 time steps of the TVM-NH and then the oceanic model is called again. The TVM-NH model forces the oceanic model with the wind stress (τ)obtained by Eq. 18 and the ocean heat flux (Q_{ocean}). The surface heat flux (Q) used by the oceanic model in Eq. 4 is calculated from the ocean heat flux of the atmospheric model (Q_{ocean}) as follows:

$$Q = \frac{Q_{ocean}}{\rho^{air} C_p} \tag{19}$$

The oceanic model then updates the SST field and returns to the TVM-NH model.

Figure 6 shows the schematic representation of the models coupling. The upper layer of the oceanic model interacts with the atmospheric model through the turbulent fluxes (determining the SST for the atmospheric model and receiving the surface heat flux and the wind stress) and with the lower layer of the oceanic model through the source or sink of heat across the interface (s). Then the oceanic model sets the currents, temperature and thickness of the upper layer. The atmospheric model uses the SST determined by the oceanic model to evaluate the turbulent fluxes at the superficial layer.

4 Results

First, the boundary condition was tested for all the main wind directions. Then, several experiments were performed with distinct goals, forming three sets of experiments. The first set was performed to test the oceanic model capability to represent the upwelling phenomenon

Table 2 Summary of the simulations discussed in this work

Simulation	Description	Domain (km)	Horizontal grid points	Wind direction	Coastline
Oceanic model					
1 to 4	Boundary 1D	180 × 180	101 × 101	E, N, S, W	Idealized
5 to 8	Boundary 2D	360 × 360	201 × 201	E, N, S, W	Idealized
9, 10	Upwelling 1D	180 × 180	101 × 101	NE, SW	Idealized
11, 12	Upwelling 2D	360 × 360	201 × 201	NE, SW	Idealized
13	Upwelling	205 × 205	50 × 50	NE	Realistic
17	Downwelling	205 × 205	50 × 50	SW	Realistic
Simulation	Description	Domain (km)	Horizontal grid points	Geostrophic wind direction	Topography and coastline
Atmospheric model					
14	Uncoupled	205 × 205	50 × 50	NE	Realistic
Coupled models					
15	Upwelling	205 × 205	50 × 50	NE	Realistic
16	Downwelling	205 × 205	50 × 50	SW	Realistic

The time step for the oceanic model is 600s and for the atmospheric model is 30s. The initial wind velocity is $6\,\mathrm{m\,s^{-1}}$

at Cabo Frio. The second set of experiments used only the atmospheric model TVM-NH and the third one used the coupled model. The experiments are summarized in Table 2.

4.1 Oceanic model: validation of the boundary conditions

One difficult problem when solving the hydrodynamic equations inside a bounded region is the correct formulation of boundary conditions. The open boundary conditions will determine, together with the differential equations themselves, the form of the interior solution, and, if not carefully chosen, they can lead to unrealistic solutions for the interior points. Therefore, several numerical experiments were performed to validate the oceanic boundary conditions.

The first set, hereafter called **1D** experiment (Simulations 1–4, 9 and 10 in Table 2), uses a domain of 180 × 180 km with 101 grid points in both directions (from 90 to 270 km, Fig. 7) and the second one, hereafter called 2D experiment (Simulations 5–8, 11 and 12), uses a larger area (360 × 360 km and 201 grid points) to minimize the boundary influence on the central area of the domain. The central area of the 2D experiment is compared to the total area of the 1D experiment. These experiments correspond to an idealized coastline with some resemblance to the realistic coastline (Fig. 2).

Figures 8 and 9 show the resulting SST fields after 4 days of integration forcing the oceanic model with a constant wind of $6\,\mathrm{ms^{-1}}$ and different directions (Simulations 1–12), for the 1D experiment on the left column of the figure and for the central area of the 2D experiment on the middle column. The average wind intensity at Cabo Frio is $6\,\mathrm{ms^{-1}}$ [13]. The integration period of 4 days was chosen because a period of 2 days is necessary for the oceanic model to present a SST field that represents the coastal upwelling phenomenon and 48 h is the duration of the coupled experiment. So the oceanic model was run for 4 days.

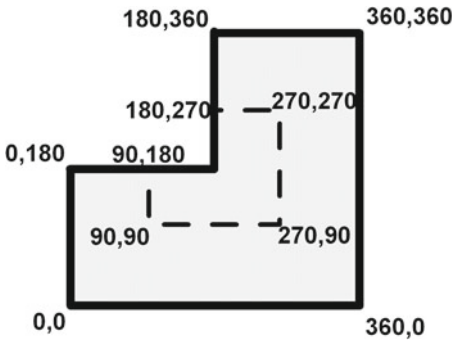

Fig. 7 Boundary condition experiment domains. The 1D experiment area is delimited by the dashed line and the outside domain delimits the 2D experiment domain

Comparing the left and central columns of Figs. 8 and 9, it is possible to notice the influence of the boundary at the SST values. However, the difference between the 1D and 2D experiments is small, never greater than 1°C. At the central area, the difference is even smaller. Given that the boundary experiments used the same integration time needed for the coupled experiment and that the analyzed area for the coupled experiment is the central area, the boundaries proved to be weakly-reflective—as expected—and therefore the results were found satisfying.

The results also show the SST expected response for each wind forcing. Figure 8a–c (Simulations 1 and 5) corresponds to the easterly wind forcing. The wind stress component parallel to the left part of the domain has the coast on its right side and, in the Southern Hemisphere it forces the Ekman transport away from the coast (Fig. 1a), causing coastal upwelling and cold SST anomalies, as expected. As the Ekman transport happens offshore, it causes water from the top of the domain—near the N–S oriented coast—to move southward, increasing upwelling at this area (Fig. 8c). In this case the SST negative anomaly and upwelling position are consistent with observations.

Figure 8d–f corresponds to the northerly wind forcing (Simulations 2 and 6). The wind stress component parallel to the coast at the right part of the domain causes also upwelling, but it is weaker than the easterly wind case because, at the left part of the domain, the wind blows from continent to ocean and, as the Ekman transport is directed offshore at the top of the domain, the currents do not go around the cape (Fig. 8f). Even though the intensity of the cold SST matches the previous case, the upwelling plume is misplaced.

The southerly wind forcing (Simulations 3 and 7) is shown in Fig. 8g–i. In this case, the wind stress component parallel to the coast at the right part of the domain has the coast on its left side, forcing the Ekman transport towards the coast, causing downwelling (Fig. 1b) and inhibiting the upwelling, as expected.

The westerly wind forcing (Simulations 4 and 8) presents the same downwelling event as in Fig. 8g, but more intense (Fig. 8j–l) because, in this case, as the wind blows from the continent to the ocean at the left part of the domain, the Ekman transport from the ocean to the continent causes the currents to go around the cape, causing downwelling also at the top of the domain (Fig. 8l).

As explained before, due to the SASH over the Atlantic Ocean, the wind field at Cabo Frio is from northeast most of the year, favoring the coastal upwelling. On the other hand, the cold front passage changes the wind field to southwesterly winds, increasing the SST value [15]. In these two cases, the wind comes from a corner of the domain (upper right for northeasterly and lower left for southwesterly wind). So, to assure that the boundary effects are not affecting the numerical solution inside the domain four more tests were performed to analyze the

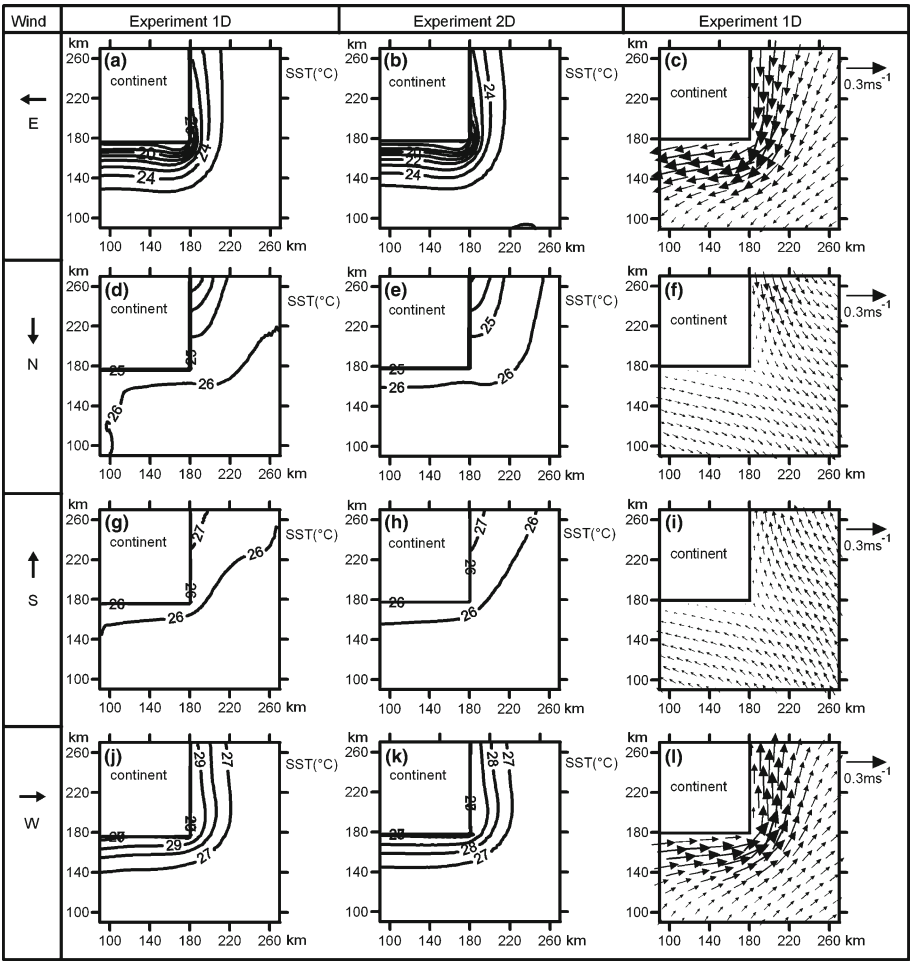

Fig. 8 Oceanic fields generated after 4 days forced by easterly winds **a** SST field in the 1D experiment (Simulation 1), **b** SST field in the central area of the 2D experiment (Simulation 5) and **c** oceanic current field in the 1D experiment (Simulation 1). Oceanic fields generated after 4 days forced by northerly winds **d** SST field in the 1D experiment (Simulation 2), **e** SST field in the central area of the 2D experiment (Simulation 6) and **f** oceanic current field in the 1D experiment (Simulation 2). Oceanic fields generated after 4 days forced by southerly winds, **g** SST field in the 1D experiment (Simulation 3), **h** SST field in the central area of the 2D experiment (Simulation 7) and **i** oceanic current field in the 1D experiment (Simulation 3). Oceanic fields generated after 4 days forced by westerly winds, **j** SST field in the 1D experiment (Simulation 4), **k** SST field in the central area of the 2D experiment (Simulation 8) and **l** oceanic current field in the 1D experiment (Simulation 4). Contour interval is 1°C

oceanic model response to northeasterly and southwesterly wind fields (Simulations 9–12, Table 2).

Figure 9a–c (northeasterly wind, Simulations 9 and 11) presents an SST field similar to the one in Fig. 8a, although now the upwelling is more intense at the top part of the domain due to the northerly wind, as shown in Fig. 8d. However, the upwelling at the bottom part of the domain is less intense than on Fig. 8a, since the wind stress component parallel to the coast is weaker. Figure 9d–f (southwesterly wind, Simulations 10 and 12) has a similar

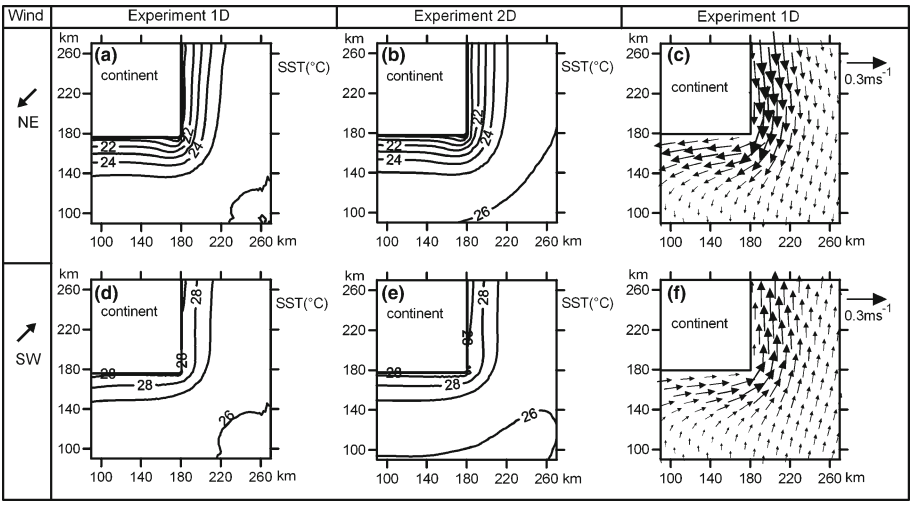

Fig. 9 Oceanic fields generated after 4 days forced by constant northeasterly winds **a** SST field in the 1D experiment (Simulation 9), **b** SST field in the central area of the 2D experiment (Simulation 11) and **c** oceanic current field in the 1D experiment (Simulation 9). Oceanic fields generated after 4 days forced by constant southwesterly winds **d** SST field in the 1D experiment (Simulation 10), **e** SST field in the central area of the 2D experiment (Simulation 12) and **f** oceanic current field in the 1D experiment (Simulation 10). Contour interval is 1°C

pattern to Fig. 8j, given that the southerly wind does not change the SST much, as shown in Fig. 8g. Again, the wind stress component parallel to the coast at Fig. 9d is weaker than at Fig. 8j, so the downwelling is less intense in the first case.

4.2 Oceanic model: representation of an upwelling event

Since the boundary conditions of the oceanic model were found satisfactory and the model produced the expected wind forcing response, an experiment was performed to generate an upwelling event representative of the SST field (Simulation 13). In this case, it is used a realistic coastline of Cabo Frio with a domain of 205 × 205 km representing the area from 21.8°S to 23.8°S and 41°W to 43.05°W (Fig. 2). The results are displayed for the central area marked by the square at Fig. 2 (latitude from 23.28°S to 22.28°S and longitude from 41.55°W to 42.55°W). The grid spacing is 3 km at a central area of 99 × 99 km and increases with a geometric progression with a ratio of 1.2 towards each boundary. This grid spacing was chosen to match the one used by the atmospheric model TVM-NH.

Figure 10 shows the SST field generated by the oceanic model after 2 days of integration forced by a constant NE wind field of 6 ms^{-1} (Simulation 13). The upwelling is stronger just west of the cape, where the coastline is E–W and the wind component parallel to the coast is also stronger. With the change in the direction of the coastline to N–S the SST is warmer, because the strongest wind component is normal to the coastline. At the upper right part of the domain, the SST drops again, since the wind is mainly parallel to the coast. These results are consistent with observations of satellite images of the region during upwelling events [2,13,17].

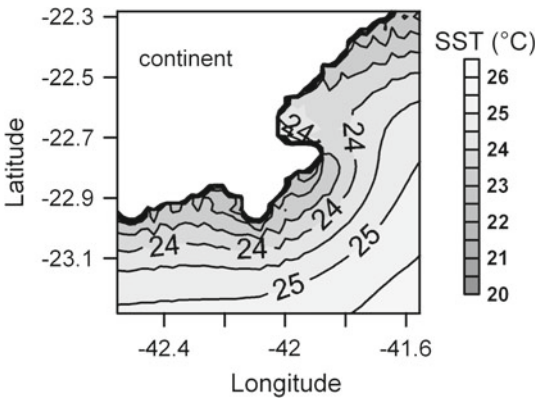

Fig. 10 SST field after 2 days of integration of the oceanic model only (Simulation 13). Contour interval is 0.5°C

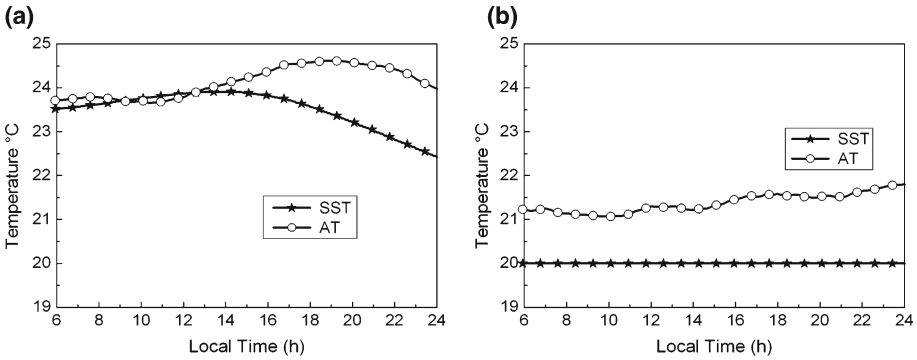

Fig. 11 Time series of SST and air temperature (AT) at 15 m height over point "A" using **a** coupled models (Simulation 15) and **b** just the atmospheric model (Simulation 14)

4.3 Response of the atmospheric model to the oceanic model

To analyze the differences between the results generated using just the atmospheric model and using the coupled model, two experiments were performed: the first one (Simulation 14) used only the atmospheric model TVM-NH with an SST field constant in space and time and equal to 20°C. The second experiment (Simulation 15) used the coupled model, with an initial SST field equal to the one displayed on Fig. 10 (Simulation 13).

Figure 11 shows the SST and air temperature (AT) time series, at 15 m of height, over point "A" of Fig. 2 for the two experiments. The air temperature of Simulation 15 (Fig. 11a) is about 3°C higher than the air temperature of Simulation 14 (Fig. 11b). The SST does not change during Simulation 14 because there is no physical mechanism able to change it in the uncoupled experiment. Therefore, the air temperature is always higher than the SST of Simulation 14. On the other hand, the air temperature of the coupled experiment (Simulation 15) is lower than the SST between 09 LT (Local Time) and 13 LT.

The major difference between the two experiments is the humidity value. The mixing ratio near the surface of the ocean is a function of the water temperature and the SST is lower on Simulation 14 (Fig. 11b) than on Simulation 15 (Fig. 11a), leading to lower values of mixing ratio on Simulation 14 than on Simulation 15 (Fig. 12). This will cause a

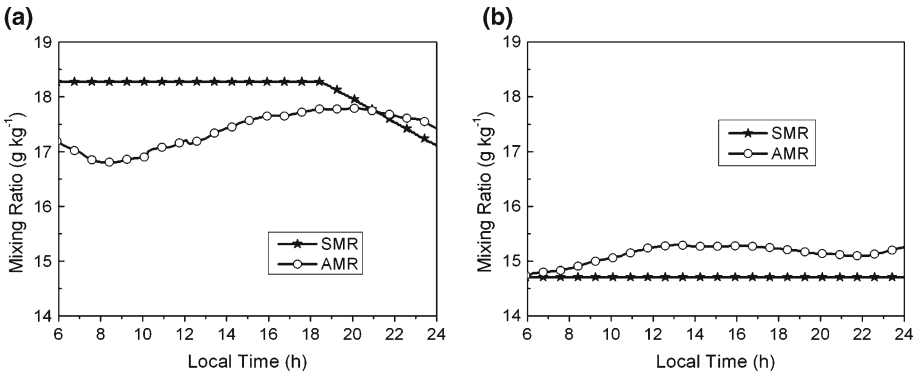

Fig. 12 Time series of mixing ratio near the surface (SMR) and at 15 m height (AMR) over point "A" using **a** coupled models (Simulation 15) and **b** just the atmospheric model (Simulation 14)

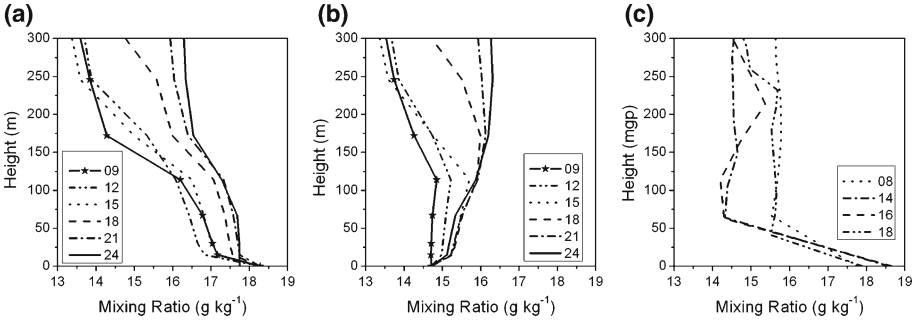

Fig. 13 Mixing ratio vertical profiles, for different times, over point "A" **a** using coupled models (Simulation 15), **b** using just the atmospheric model (Simulation 14) and **c** obtained by radiosonde sounding by Oda [17] at 01/12/1995

great discrepancy on the content of water of the atmosphere between the two experiments, as shown in Fig. 12 that presents the mixing ratio time series over the point "A" for both experiments near the surface (1 mm above the ocean surface) and at 15 m of height. The mixing ratio is the ratio of the mass of water vapor per kilogram of dry air at a given pressure.

Figure 13 presents the mixing ratio vertical profiles over the point "A" for both experiments and an observational mixing ratio vertical profile for different times. As expected, Simulation 15 presents higher values of mixing ratio near the sea surface (Fig. 13a) and these values decrease with height, but Simulation 14 (Fig. 13b) shows lower values of mixing ratio at the sea surface than at higher altitudes.

The mixing ratio vertical profiles provided by radiosonde soundings taken by Oda [17] on 01/12/1995 are displayed in Fig. 13c. It is noticeable that the coupled experiment Simulation 15 (Fig. 13a) is a much better approximation of the water content in the atmosphere than Simulation 14 (Fig. 13b), since the values of the mixing ratio near the surface presented by the soundings (Fig. 13c) are closer to the values presented by Simulation 15 and the mixing ratio values decrease with height, just like the values of the coupled experiment (Simulation 15).

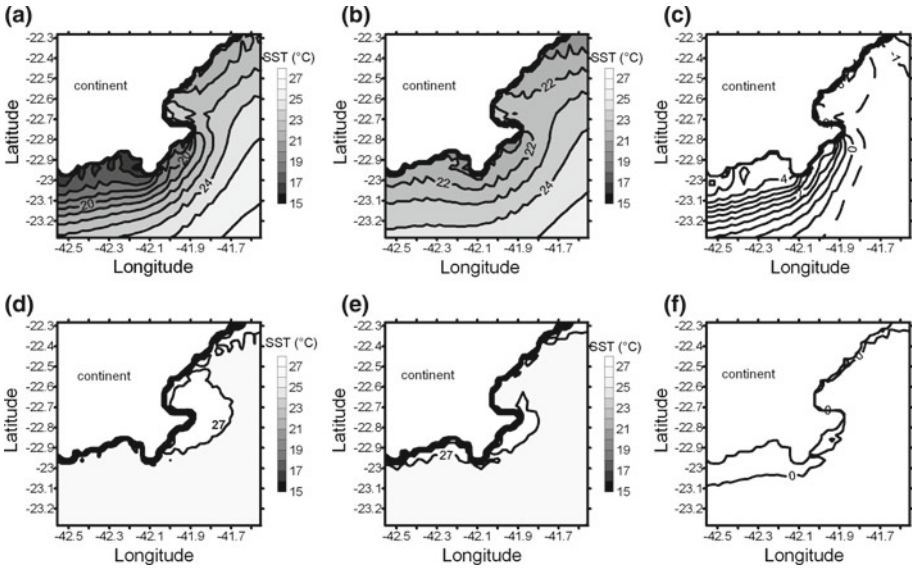

Fig. 14 SST field with initial northeasterly wind forcing after 2 days of integration of the **a** coupled model (Simulation 16), **b** oceanic model forced by a constant 6 ms^{-1} wind field (Simulation 14) and **c** difference between the oceanic model and the coupled models. The SST field with initial southwesterly wind forcing after 2 days of integration of the **d** coupled model (Simulation 17), **e** oceanic model forced by a constant 6 ms^{-1} wind field (Simulation 18) and **f** difference between the oceanic model and the coupled model. Contour interval for **a**, **b**, **d**, **e** is 1°C and for **c**, **f** is 0.5°C. *Dashed lines* represent negative values

4.4 Oceanic model response to the atmospheric model

Two experiments were performed with the coupled model (Simulations 15 and 16) to analyze the oceanic response to the atmospheric model. The first one used a NE geostrophic wind of 6 ms^{-1} as initial condition, in order to represent an upwelling favorable situation (Simulation 15), and the second one used an initial SW geostrophic wind of 6 ms^{-1} (Simulation 16), zonal and meridional components equal to 4.24 ms^{-1} at all heights, to represent the passage of a cold front (downwelling situation).

Then, to compare the coupled results with the uncoupled ones, two more experiments were performed using just the oceanic model. The first one was Simulation 13 (constant NE wind of 6 ms^{-1}), but performed for two more days after the initial period that generated Fig. 10, and the second one used a constant SW wind of 6 ms^{-1} (Simulation 17). All the experiments used the SST field represented by Fig. 10 as initial SST field.

Figure 14a, d shows the SST field after 2 days of integration of the coupled model for a geostrophic NE wind (Fig. 14a—Simulation 15) and for geostrophic SW wind (Fig. 14d—Simulation 16) and Fig. 14b, e shows the SST field after 2 days of integration of the oceanic model for constant 6 ms^{-1} NE wind (Fig. 14b—Simulation 13) and for constant 6 ms^{-1} SW wind (Fig. 14e—Simulation 17). Comparing to the initial SST field (Fig. 10), it is noticeable that the experiment with NE wind (Fig. 14a) enhanced the upwelling signal, since the SST decreased $4 - 5$°C near the coast, at latitudes of approximately 23°S. Near the coast at latitudes from 22.7°S to 22.6°S the SST remained the same, because the wind is mostly normal to the coastline at this area. On the other hand, the SW wind (Fig. 14b) disrupted the upwelling phenomenon, increasing the SST all over the domain.

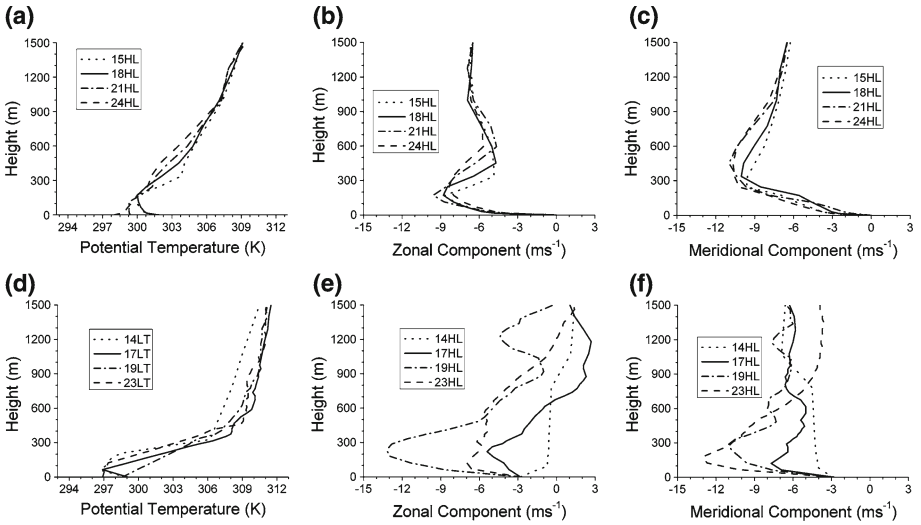

Fig. 15 Vertical profiles generated by Simulation 15 (upwelling event) of **a** air potential temperature, **b** zonal and **c** meridional components of the wind. Vertical profiles observed by Oda [17], at 08/04/1995, in (22.97°S, 42.03°W) of **d** air potential temperature, **e** zonal and **f** meridional components of the wind

The difference between the uncoupled (Simulations 13 and 17) and the coupled (Simulations 15 and 16) SST field results is displayed in Fig. 14c, f. For the NE wind forcing (Fig. 14c), the difference between the experiments is up to 4°C near the coast at the western part of the domain, and it is negative up to 1°C at the eastern part of the domain. This difference happens because of the sea-breeze circulation, that is resolved only at the coupled experiment and rotates the wind clockwise, making it more parallel to the coast at the western part and more normal to the coast at the eastern part of the domain. This result suggests that the sea-breeze increases the upwelling intensity westward of Cabo Frio, as it was proposed by Franchito et al. [13]. For the SW wind forcing (Fig. 14f), the difference between the experiments is never greater than 0.5°C.

4.5 Coupled model results

The coupling of the models allows a more realistic investigation of the circulations at Cabo Frio. Figure 15 shows the vertical profiles of air potential temperature and wind components that were generated by the coupled model and taken by radiosonde soundings by Oda [17] at 01/09/1995, over the continent and near the coastline at (22.97°S, 42.03°W). The observed air potential temperature profile (Fig. 15d) presents a more stable atmosphere than the generated profile (Fig. 15a). However, both profiles present a similar height for the ABL (approximately 200 m between 14 and 15 LT). The wind component vertical profiles generated by the model (Fig. 15b, c) are similar to the observed profiles (Fig. 15e, f) and present an interesting feature: a NE low level jet with maximum speed between 200 and 300 m of altitude.

For the downwelling event (Simulation 16), the air potential temperature vertical profile (Fig. 16a, d) in (22.97°S, 42.03°W) shows a more unstable atmosphere than for the upwelling event (Fig. 15a, d). It is important to notice that the measurements taken by Oda [17] occurred during the winter (08/04/1995) and therefore present lower temperatures than the simulation. The wind profiles (Fig. 16b, c, e, f) show once again the presence of a low level jet between 200 and 300 m of altitude, but its direction is now from SW.

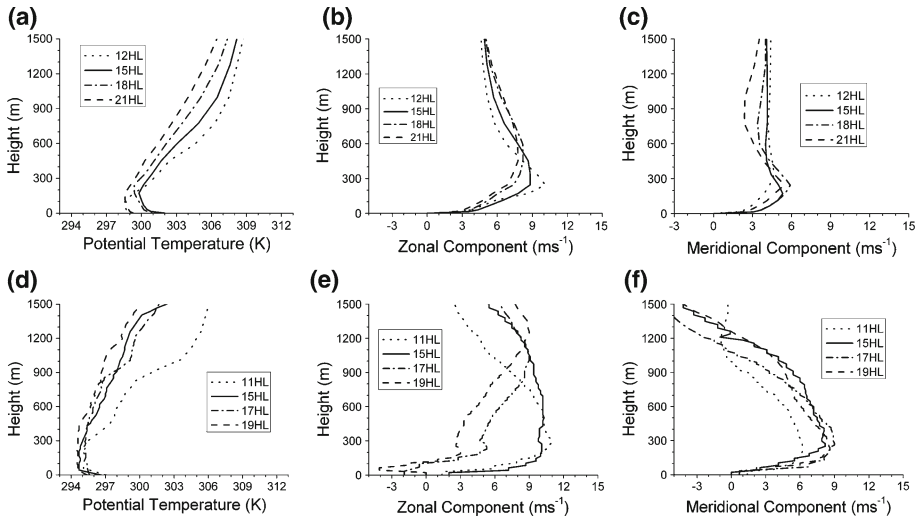

Fig. 16 Vertical profiles generated by Simulation 16 (downwelling event) of **a** air potential temperature, **b** zonal and **c** meridional component of the wind. Vertical profiles observed by Oda [17], at 08/04/1995, in (22.97°S, 42.03°W) of **d** air potential temperature, **e** zonal and **f** meridional components of the wind

5 Conclusions

The main objective of this work was to investigate the capability of an oceanic numerical model, dynamic and thermodynamically coupled to a three-dimensional mesoscale atmospheric numerical model, to simulate the basic features of the air–sea interaction in the coastal upwelling area of Cabo Frio (RJ, Brazil). The oceanic upwelling/downwelling regime is an important feature in the oceanic circulation of Cabo Frio and determines the sustainability of local ecosystems. This regime is predominantly driven by the atmospheric circulation and is well documented, being suitable to be used as test reference for atmospheric and oceanic coupled and uncoupled models.

The oceanic model presented here proved to have a weakly-reflective boundary condition and was able to produce an SST field that represents the coastal upwelling/downwelling regime at Cabo Frio with constant northeasterly/southwesterly wind forcing. It was also successfully coupled to the TVM-NH atmospheric model.

Concerning the response of the atmospheric model to the oceanic forcing, it was observed that there are considerable differences between the coupled model result and the result generated by the atmospheric model forced by a constant and uniform SST field, especially on the water content of the atmosphere. When comparing the model results with observations of the mixing ratio vertical profile at Cabo Frio, it was found that the coupled model results generate a better fit than the uncoupled atmospheric model results.

The oceanic model response to the atmospheric forcing also presented differences between the experiments using the coupled model and just the oceanic model forced by constant wind fields. For the NE wind forcing case the coupled model, showed more realistic results, with an increase of upwelling phenomenon intensity (decrease of SST up to 4°C) westward from the cape, in comparison with the SST field produced by the uncoupled oceanic model, indicating that the sea-breeze generated by the atmospheric model is responsible for this intensification, as it was already suggested by other researchers [13,17]. For the downwelling event, SW wind forcing case, the difference between the experiments was smaller (<0.5°C).

Analyzing the results of the coupled model, it was noticed that the vertical profiles of air potential temperature and wind components generated by the model are similar to the observations and are able to represent the formation of a low level jet, a particular feature of the circulation in Cabo Frio, with the same direction as the geostrophic wind (from NE for the upwelling case and from SW for the downwelling case).

The results showed in this work indicate that the coupled model provides a better analysis of the oceanic, atmospheric and interface processes at Cabo Frio.

Acknowledgements We thank the Brazilian Research Agency CNPq (Grant 142007/2005-6 and 305854/2003-8) for funding this work and Tania Ocimoto Oda for providing the data of radiosonde soundings used in it. We also thank the support given by the Fundação de Amparo à Pesquisa do Estado de São Paulo (FAPESP).

References

1. Amor CC (2004) Intrusões da Água Central do Atlântico Sul sobre a Plataforma Continental situada entre a Ilha de São Sebastião (SP) e o Cabo de São Tomé (RJ). Thesis, University of São Paulo, Brazil (in Portuguese)
2. Rodrigues RR, Lorenzzetti JA (2001) A numerical study of the effects of bottom topography and coastline geometry on the Southeast Brazilian coastal upwelling. Cont Shelf Res. doi:10.1016/S0278-4343(00)00094-7
3. Guimarães MA, Paiva AM, Coutinho R (2005) Modeling *Ulva* spp. dynamics in a tropical upwelling region. Ecol Model. doi:10.1016/j.ecolmodel.2005.04.023
4. Carbonel CAAH, Valentin JL (1996) Numerical modeling of phytoplankton bloom in the upwelling ecosystem of Cabo Frio (Brasil). Ecol Model. doi:10.1016/S0304-3800(98)00201-4
5. Diniz AG, Hamacher C, Wagener ALR, Rodriguez-Gonzalez E (2003) Is copper inhibiting factor for primary production in the upwelling waters of Cabo Frio. J Braz Chem Soc 14(5):815–821
6. Mahiques MM, Bicego MC, Silveira ICA, Sousa SHM, Lourenço RA, Fukumoto MM (2005) Modern sedimentation in the Cabo Frio upwelling system, Southeastern Brazilian Shelf. An Acad Bras Ciênc 77:535–548
7. Gilliam RC, Raman S, Niyogi DDS (2004) Observational and numerical study on the influence of large-scale flow directions and coastline shape on sea-breeze evolution. Boundary-Layer Meteorol 111:275–300
8. Talbot C, Augustin P, Leroy C, Willart V, Delbarre H, Khomenko G (2007) Impact of a sea breeze on the boundary-layer dynamics and the atmospheric stratification in a coastal area of the North Sea. Boundary-Layer Meteorol 125:133–154
9. Bastin S, Drobinski P (2006) Sea-breeze-induced mass transport over complex terrain in south-eastern France: A case-study. Q J R Meteorol Soc 132: 405–423. doi:10.1256/qj.04.111
10. Bouchlaghem K, Mansour FB, Elouragini S (2007) Impact of a sea breeze event on air pollution at the Eastern Tunisian Coast. Atmos Res 86: 162–172. doi:10.1016/j.atmosres.2007.03.010
11. Clappier A, Martilli A, Grossi P, Thunis P, Pasi F, Krueger BC, Calpini B, Graziani G, VanDen Bergh H (2000) Effect of sea breeze on air pollution in the greater Athens Area. Part I: Numerical simulations and field observations. J Appl Meteorol 39:546–562
12. Carbonel CAAH (2003) Modelling of upwelling-downwelling cycles caused by variable wind in a very sensitive coastal system. Cont Shelf Res 23: 1559–1578. doi:10.1016/S0278-4343(03)00145-6
13. Franchito SH, Rao VB, Stech JL, Lorenzzetti JA (1998) The effect of coastal upwelling on the sea-breeze circulation at Cabo Frio, Brazil: a numerical experiment. Ann Geophys 16:866–881
14. Ikeda Y, Miranda LB, Rock NJ (1974) Observations on stages of upwelling in the region of Cabo Frio (Brazil) as conducted by continuous surface temperature and salinity measurements. Bol Inst Oceanogr 23:33–46
15. Castro BM (1996) Correntes e massas de água na Plataforma Continental Norte de São Paulo. Thesis, University of São Paulo, Brazil (in Portuguese)
16. Leite JRB (2005) Correntes na Plataforma Continental ao largo de Arraial do Cabo (RJ): medições com perfilador acústico (ADCP). Dissertation, University of São Paulo, Brazil (in Portuguese)
17. Oda TO (1997) Influencia da ressurgência costeira sobre a circulação local em Cabo Frio (RJ). Dissertation, INPE, Brazil (in Portuguese)
18. Dourado M, Oliveira AP (2001) Observational description of the atmospheric and oceanic boundary layer over the Atlantic Ocean. Rev Bras Oceanogr 49:49–59

19. Dourado M, Oliveira AP (2008) A numerical investigation of the atmosphere-ocean thermal contrast over the coastal upwelling region of Cabo Frio, Brazil. Atmosfera 21:13–34
20. McCreary IP, Kundu P (1988) A numerical investigation of the Somali Current during the Southwest Monsoon. J Mar Res 46(1):25–58
21. McCreary IP, Lee HS, Enfield DB (1989) The response of the coastal ocean to strong offshore winds: with application to circulations in the Gulfs of Tehuantepec and Papagayo. J Mar Res 47(1):81–109
22. McCreary JP, Zhang S, Shetye SR (1997) Coastal circulation driven by river outflow in a variable-density 1-1/2 layer model. J Geophys Res 102(C7):15535–15554
23. O'Brien JJ, Hurlburt HE (1972) A numerical model of coastal upwelling. J Phys Oceanogr 2:14–26
24. O'Brien JJ, Clancy RM, Clarke AJ, Crepon M, Elsberry R, Gammelsrod T, MacVean M, Røed LP, Thompson JD (1977) Upwelling in the ocean: two and three dimensional models of upper ocean dynamics and variability. In: Kraus EB (ed) Modelling and prediction of the upper layers of the ocean. Pergamon Press, New York, pp 178–228
25. Røed LP, Shi XB (1999) A numerical study of the dynamics and energetics of cool filaments, jets, and eddies off the Iberian Peninsula. J Geophys Res 104(C12):29817–29841
26. Verboom GK, Slob A (1984) Weakly reflective boundary conditions for two-dimensional shallow water flow problems. Publication no. 322. Delft Laboratory
27. Van Dongeren AR, Svendsen IA (1997) Absorbing-generating boundary condition for shallow water models. J Waterw Port Coast Ocean Eng 123:303–313
28. Bornstein RD (1975) The two-dimensional URBMET urban boundary layer model. J Appl Meteorol 14:1459–1477
29. Bornstein R D, Cordova J, Salvador R, Shieh LJ (1991) Modeling the polluted coastal urban environment, vol 3. Report EA-5091, research project 1630-13. Electric Power Research Institute EPRI, 235 pp
30. Schayes G, Thunis P (1990) The three-dimensional mesoscale model in vorticity mode (TVM). Contribution no. 60. Institut d'Astronomie et de Geophysique Georges Lemaitre, Université Catholique de Louvain, Louvein-la-Neuve, Belgium, 42 pp
31. Bornstein RD, Thunis P, Grossi P, Schayes G (1996) Topographic vorticity-mode mesoscale-β (TVM) model. Part II: Evaluation. J Appl Meteorol 35:1824–1834
32. Schayes G, Thunis P, Bornstein R (1996) Topographic vorticity mesoscale-β (TVM) model. Part I: Formulation. J Appl Meteorol 35:1815–1823
33. Thunis P, Clappier A (2000) Formulation and evaluation of a nonhydrostatic mesoscale vorticity model (TVM). Mon Weather Rev 128:3236–3251
34. Martin F, Crespí SN, Palacios M (2001) Simulation of mesoscale circulation in the center of the iberian peninsula for thermal low conditions. Part I: Evaluation of the topography vorticity-mode mesoscale model. J Appl Meteorol 40:880–904
35. Martin F, Palacios M, Crespí SN (2001) Simulation of mesoscale circulation in the center of the iberian peninsula for thermal low conditions. Part II: Air-parcel transport patterns. J Appl Meteorol 40:905–914
36. Karam HA (2002) Estudo Numérico dos Jatos de Baixos Níveis e suas Implicações na Dispersão de Poluentes no Estado de São Paulo. Thesis, University of Sao Paulo, Brazil (in Portuguese)
37. Morais MVB (2010) Investigação da camada limite planetária sobre a região urbana de São Paulo por meio do modelo de mesoescala TVM acoplado ao modelo do dossel urbano de Martilli. Dissertation, University of Sao Paulo, Brazil (in Portuguese)
38. Pereira MMR (2004) Estudo do Transporte Local de Poluentes em Iperó por meio de um Modelo Lagrangiano de Partículas. Thesis, University of Sao Paulo, Brazil (in Portuguese)
39. Pereira de Sousa ON (2006) Investigação do papel da topografia e ocupação do solo na camada limite planetária sobre a cidade de São Paulo. Dissertation, University of Sao Paulo, Brazil (in Portuguese)
40. Stivari SMS, Oliveira AP, Karam HA, Soares J (2003) Patterns of local circulation in the Itaipu Lake area: numerical simulations of lake breeze. J Appl Meteorol 42:37–50
41. Deardorff JW (1978) Efficient prediction of ground surface temperature and moisture with inclusion of a layer of vegetation. J Geophys Res 83:1889–1903
42. Targino ACL, Soares J (2002) Modeling surface energy-fluxes for Ipero, SP, Brazil: an approach using numerical inversion. Atmos Res 63:101–121
43. Orgaz MDM, Fortes JL (1998) Estudo das brisas costeiras na região de Aveiro. In: Proceedings do 1^0 Simpósio de Meteorologia e Geofísica Hispano Português. Lagos, Portugal (in Portuguese)
44. Belward AS (ed) (1996) The IGBP-DIS Global 1 km Land Cover Data Set (DISCover): proposal and implementation plans. IGBP-DIS working paper no. 13. Toulouse, France, 61 pp